

## Structural, Magnetic and $^{151}\text{Eu}$ Mössbauer Studies of Mechano-synthesized Nanocrystalline $\text{EuCr}_{1-x}\text{Fe}_x\text{O}_3$ Particles

H. M. Widatallah<sup>1,\*</sup>, T. M. Al-Shahumi<sup>1</sup>, Z. Klencsár<sup>2</sup>, M. Pekala<sup>3</sup>, A. M. Gismelseed<sup>1</sup>, I. A. Al-Omari<sup>1</sup>, A. D. Al-Rawas<sup>1</sup> and D. Seifu<sup>4</sup>

<sup>1</sup>Department of physics, Sultan Qaboos University, P. O. Box 36, 123, Muscat, Oman;

<sup>2</sup>Research Centre for Natural Sciences, Hungarian Academy of Sciences, Pusztaszeri út 59-67, Budapest, 1025, Hungary; <sup>3</sup>Chemistry Department, University of Warsaw, 101, PL-02-089, Warsaw, Poland; <sup>4</sup>Department of Physics, Morgan State University, Baltimore, MD 21251, USA;

\*Email: [hishammw@squ.edu.om](mailto:hishammw@squ.edu.om); Tel: +968-9953932; Fax: +968 24414228

### Abstract

We report on the mechanosynthesis of single-phased  $\text{EuCr}_{1-x}\text{Fe}_x\text{O}_3$  ( $x = 0.0, 0.1, 0.3, 0.5, 0.7, 0.9,$  and  $1.0$ ) nanocrystalline particles ( $\sim 20\text{-}50$  nm) at temperatures that are significantly lower than those at which the corresponding bulk materials are conventionally synthesized and their structural and magnetic characterization. The average crystallite size was found to decrease, the lattice parameters increase, and the unit cell gets more distorted with increasing  $x$ . All samples showed weak ferromagnetism due to spin canting. The Curie temperatures, though increase with increasing  $x$ , are significantly lower than those of the corresponding bulk materials. Simple Curie-Weiss fits for the paramagnetic susceptibilities were found to be more physically plausible relative to fits where Vleck-type contributions to the paramagnetic susceptibilities due to  $\text{Eu}^{3+}$  ionic sublattices, that are separate from of the  $\text{Cr}^{3+}/\text{Fe}^{3+}$  ones, were assumed. The non-existence of such separate  $\text{Eu}^{3+}$  and  $\text{Cr}^{3+}/\text{Fe}^{3+}$  sublattices was further supported by  $^{151}\text{Eu}$  Mössbauer spectra of the nanoparticles which favor a non-equilibrium cation distribution wherein a considerable amount of  $\text{Eu}^{3+}$  and  $\text{Cr}^{3+}/\text{Fe}^{3+}$  ions exchange their normal dodecahedral and octahedral perovskite-related sites, respectively. The supertransferred hyperfine magnetic field at the site of the  $^{151}\text{Eu}$  nuclei, induced by neighboring  $\text{Cr}^{3+}/\text{Fe}^{3+}$  ions, was found to be considerably larger for B-site nuclei than for A-site ones. The antisite behavior concluded in this study is consistent with  $^{57}\text{Fe}$  Mössbauer spectral analysis of the nanoparticles that favor the presence of the majority of the  $\text{Fe}^{3+}$  ions at the usual B-sites and minority  $\text{Fe}^{3+}$  ions either at the A-sites or at B-sites with  $\text{Eu}^{3+} / \text{Cr}^{3+}$  nearest B-site neighbors. The relative site occupancies associated with the cationic site exchange inferred from both the  $^{151}\text{Eu}$  and  $^{57}\text{Fe}$  Mössbauer spectra are remarkably consistent.

## 1- Introduction.

The physical properties of europium orthoferrite ( $\text{EuFeO}_3$ ) and europium orthochromite ( $\text{EuCrO}_3$ ) render them attractive in many applications including solid oxide fuel cells, catalysis, chemical sensing and optical communications [1-9]. Both materials crystallize in an orthorhombically distorted perovskite structure (space group  $Pbnm$ ) and have very similar lattice parameters, bond distances and angles [8,10]. The distortion from the ideal cubic perovskite structure is mainly in the dodecahedral A-sites that are occupied by the rare earth ( $\text{Eu}^{3+}$ ) ion. The transition metal ions ( $\text{Fe}^{3+}$  and  $\text{Cr}^{3+}$ ) occupy the octahedral B-sites which are less distorted by virtue of their rotation [9,11]. While both materials are essentially antiferromagnetic, the asymmetry of their magnetic unit cells, which is equal to that of their crystallographic unit cells, causes the alignment of the  $\text{Fe}^{3+}$  and  $\text{Cr}^{3+}$  magnetic moments to be not strictly antiparallel but slightly canted resulting in a small net magnetization and accordingly the systems exhibit a weak ferromagnetic behavior. This behavior is a consequence of the *Dzyaloshinskii-Moriya* antisymmetric exchange coupling that causes the magnetic lattices to be comprised of collinear antiferromagnetic spin order along a particular crystallographic direction and a canted spin order along another [13,14]. The Curie temperatures ( $T_C$ ) of  $\text{EuFeO}_3$  and  $\text{EuCrO}_3$  associated with this weak ferromagnetism are 662 K and 181 K, respectively [4,13]. The effect of partial cationic substitution of  $\text{Fe}^{3+}$  in  $\text{EuFeO}_3$  with  $\text{Ca}^{2+}$ ,  $\text{Mn}^{3+}$ ,  $\text{Co}^{3+}$ ,  $\text{Sc}^{3+}$  and  $\text{Cr}^{3+}$ , for instance, on the structural and magnetic properties of the material has been studied by several workers [10,15-18]. Fewer studies, however, have been reported on the partial substitution of the  $\text{Cr}^{3+}$  ion in  $\text{EuCrO}_3$  by other cations. To our knowledge there is only one published study on the structure and magnetism of *bulk*  $\text{EuCr}_{1-x}\text{Fe}_x\text{O}_3$  particles prepared at  $\sim 1300^\circ\text{C}$  [16].

Motivated by ample experimental evidence that magnetic oxide nanoparticles depict novel physical properties relative to their bulk counterparts [19,20], we have for some time, been working on the low-temperature processing of pure and cation-doped magnetic oxide nanoparticles, their structures and magnetic properties [8,21-25]. Our results have confirmed high energy mechanosynthesis to be a particularly simple and reliable way for producing oxide nanoparticles that could structurally and magnetically be considerably different from their corresponding bulk. For instance we have recently shown an unusual partial A-B cationic site exchange to exist in  $\text{EuCrO}_3$  nanocrystalline particles prepared by mechanosynthesis that has not been reported for the conventionally prepared bulk solid [8]. While antisite disorder in perovskite-related structure is widely known to be induced via thermal treatment, radiation damage or cationic doping [26-29], it was interesting to see

how the same could be induced by the mechanosynthesis route. Generally it is assumed that this antisite disorder is governed by the relative cationic radii such that cations with similar size and valence state have a higher probability of occupying the “wrong” sites [30].

In this paper we show how mechanosynthesis leads to the formation of  $\text{EuCr}_{1-x}\text{Fe}_x\text{O}_3$  nanocrystalline particles at temperatures that are significantly lower than those at which the materials, in bulk form, are conventionally produced. The structural phase evolution during the formation process of the nanoparticles is systematically explored. X-ray powder diffraction (XRD), magnetic measurements and  $^{151}\text{Eu}$  Mössbauer measurements are then combined to explore their crystal structure and magnetic properties. It should be accentuated that while, in his classic work [16], Gibb has explored the structure and magnetism of *bulk*  $\text{EuCr}_{1-x}\text{Fe}_x\text{O}_3$ , this is to our knowledge the first systematic study on the formation, structure and magnetic properties of *nano-sized*  $\text{EuCr}_{1-x}\text{Fe}_x\text{O}_3$  particles. Mössbauer spectroscopy is best suited to study the structure and magnetism of the  $\text{EuCr}_{1-x}\text{Fe}_x\text{O}_3$  system as the environments of both the rare-earth ( $\text{Eu}^{3+}$ ) and transition metal ( $\text{Cr}^{3+}/\text{Fe}^{3+}$ ) ions can be probed using  $^{151}\text{Eu}$  and  $^{57}\text{Fe}$  Mössbauer spectroscopy, respectively. In our preliminary  $^{57}\text{Fe}$  Mössbauer study [25] of the present  $\text{EuCr}_{1-x}\text{Fe}_x\text{O}_3$  nanoparticles, it was proposed that the majority of the  $\text{Fe}^{3+}$  ions occupy the B-sites in the perovskite structure and the rest occupy either A-sites, or B-sites with  $\text{Eu}^{3+}$  /  $\text{Cr}^{3+}$  nearest B-site neighbors. It is, therefore, of interest to probe the immediate environment of the  $\text{Eu}^{3+}$  ions in the mechanosynthesized  $\text{EuCr}_{1-x}\text{Fe}_x\text{O}_3$  nanoparticles with  $^{151}\text{Eu}$  Mössbauer spectroscopy and find out whether they exclusively occupy their usual A-site or partly exchange sites with the B-site transition metal ions, and what implications does that have on their structural and magnetic properties.

## 2. Experimental and Methods:

Appropriate amounts of high purity *cubic*  $\text{Eu}_2\text{O}_3$ ,  $\text{Cr}_2\text{O}_3$  and  $\alpha\text{-Fe}_2\text{O}_3$  in the 1: 1-x: x molar ratio ( $x = 0.0, 0.1, 0.3, 0.5, 0.7, 0.9, 1.0$ ) were homogenously mixed in an agate mortar and then milled in air for various times using a Fritsch Pulverisette 6 planetary ball mill with tungsten carbide vial (250 ml) and balls (20 mm). The milling speed was 300 rpm and the powder-to-balls mass ratio was 1:27. For each value of  $x$  the milling process was terminated when further milling was found to bring about no tangible compositional and structural change. Each pre-milled mixture was sintered in air at different temperatures for periods of 8 h using a Carbolite (HFT 1800) furnace followed by rapid cooling in air until a single  $\text{EuCr}_{1-x}\text{Fe}_x\text{O}_3$  phase was formed. The particles' size and morphology were determined with a

JEOL 1200EX transmission electron microscope (TEM). XRD patterns were collected with a Philips PW1710 diffractometer using  $\text{CuK}\alpha$  radiation ( $\lambda = 1.5406 \text{ \AA}$ ). The XRD data were fitted with the Powdercell program based on the Le Bail pattern-decomposition method [31]. For the simple full pattern refinement using structure data, done in the present work, Powdercell applies a least square algorithm. The Le Bail procedure of the program tries to extract structure amplitudes from the de-convoluted intensities that can be used for an intuitive structure analysis. The refined structural variables were the lattice parameters and the peak widths required to estimate the crystallite size using Scherrer equation [32,33]. The temperature variation of the magnetization was recorded in the range 270 - 900 K using a Faraday balance in a magnetic field of 1.5 T at a heating rate of 4 K/min and relative accuracy better than 1%. The temperature variation of the magnetization in the range 100-840 K was measured using a commercial vibrating sample magnetometer (VSM) in a magnetic field of 1.35 T in the zero-field-cooling mode (ZFC). As no divergence was expected at high field, no magnetic measurements were made in the field-cooling (FC) mode. The Curie temperatures ( $T_C$ ) were determined from the minima of the temperature derivatives of the magnetizations.  $^{151}\text{Eu}$  transmission Mössbauer measurements were performed at room temperature on samples with  $35 \text{ mg/cm}^2$  surface density, using the 21.54 keV gamma ray provided by a 100 mCi  $^{151}\text{SmF}_3$  source. A  $\text{EuF}_3$  sample having a concentration of  $5.5 \text{ mg/cm}^2$  was used as a standard relative to which isomer shifts are quoted. Both single and simultaneous fitting of the  $^{151}\text{Eu}$  Mössbauer spectra were performed with version 4.0Pre of the MossWinn program [34], by adopting the following constants concerning the  $7/2 \rightarrow 5/2$  (21.54 keV) nuclear transition of the  $^{151}\text{Eu}$  nucleus:  $g_{7/2} = +0.740286$  for the gyromagnetic factor of the excited state,  $g_{5/2} = +1.38868$  for that of the ground state,  $Q_{7/2} = +1.28$  barn for the quadrupole moment of the excited state and  $Q_{5/2} = +0.903$  barn for that of the ground state. The constants  $g_{7/2}$  and  $g_{5/2}$  correspond, respectively, to nuclear magnetic moments of  $\mu_{7/2} = 2.591 \mu_N$  and  $\mu_{5/2} = 3.4717 \mu_N$ ; ( $\mu_N$  being the nuclear magneton). Simultaneous fitting of all the spectra is particularly useful in cases when either the physical model, or the precise value of the Mossbauer parameters cannot be derived unambiguously using a single spectrum fitting.

### 3. Results and Discussion

#### 3.1. Formation and structure

The structural and compositional phase evolution when the 1: 1-x: x molar mixtures of the *cubic* polymorph of  $\text{Eu}_2\text{O}_3$ ,  $\text{Cr}_2\text{O}_3$  and  $\alpha\text{-Fe}_2\text{O}_3$  were subjected to milling and

subsequent sintering can be envisaged by discussing the cases of the end members of the  $\text{EuCr}_{1-x}\text{Fe}_x\text{O}_3$  solid solution series, viz.  $\text{EuCrO}_3$  ( $x = 0.0$ ) and  $\text{EuFeO}_3$  ( $x = 1.0$ ). The parameters governing the formation of the other members in the series were found to gradually evolve as  $x$  increases. Figure 1 shows the XRD patterns recorded when the mixture with  $x = 0.0$  (i.e. 1: 1 molar mixture of  $\text{Eu}_2\text{O}_3$  and  $\text{Cr}_2\text{O}_3$ ) was subjected to milling for the times indicated. The XRD profile collected after 1 h of milling clearly reveals that while the reflection peaks of the  $\text{Cr}_2\text{O}_3$  component remain almost unchanged, those of the *cubic*  $\text{Eu}_2\text{O}_3$  component almost disappear. Concomitantly, very broad peaks indexable to the *monoclinic* modification of  $\text{Eu}_2\text{O}_3$  develop. Milling-induced *cubic-to-monoclinic* phase transformation in  $\text{Eu}_2\text{O}_3$  has already been observed [8,35]. Further milling of the mixture for 10 h shows the reflection peaks of both  $\text{Eu}_2\text{O}_3$  and  $\text{Cr}_2\text{O}_3$  to broaden and decrease in intensity implying a decrease in crystallinity and the fragmentation of both materials into fine particles that are tightly pressed together where both materials enjoy a large interface. The XRD profile recorded from the reactants' mixture milled for 20 h shows that milling has induced the reaction leading to the formation of  $\text{EuCrO}_3$  whose reflection peaks dominate the pattern except for small amounts of un-reacted components as the most dominant reflection peaks of  $\text{Cr}_2\text{O}_3$  indicate. With increasing milling times in steps of 10 h to 60 h and then to 75 h and finally to 120 h, the reflection peaks attributable to  $\text{EuCrO}_3$  continued to intensify and those of the initial precursors to gradually disappear. The milling process was terminated when it was apparent that a single-phased  $\text{EuCrO}_3$  phase could not be attained by milling only. Figure 2 shows the XRD patterns recorded from the 120 h pre-milled reactants' mixture with  $x = 0.0$  after sintering (8 h) at the temperatures shown. It is clear that as the temperature increases the reflection peaks of the  $\text{EuCrO}_3$  and the un-reacted phases gradually intensify and fade out, respectively. A *single perovskite-related*  $\text{EuCrO}_3$  phase was obtained at  $950^\circ\text{C}$  (8 h). This temperature is  $\sim 350^\circ\text{C}$ - $450^\circ\text{C}$  lower than those at which  $\text{EuCrO}_3$  forms using the conventional high-temperature route [4,10]. It is pertinent to mention that we have recently shown that  $\text{EuCrO}_3$  nanocrystalline particles may also form at only  $700^\circ\text{C}$  (8h) when a different milling regime is adopted [8].

The formation of the other single-phased  $\text{EuCr}_{1-x}\text{Fe}_x\text{O}_3$  particles ( $x=0.1, 0.3, 0.5, 0.7, 0.9$  and  $1.0$ ) was different from that of the material with  $x = 0.0$  ( $\text{EuCrO}_3$ ) in the following two aspects:

- (1) As the iron content ( $x$ ) increases, the pre-milling time required for inducing the reaction yielding single-phased  $\text{EuCr}_{1-x}\text{Fe}_x\text{O}_3$  particles decreases considerably. This is readily seen in Figure 3 which depicts the XRD profiles recorded from the reactants'

mixtures with the maximum iron content  $x = 1.0$  (i.e. the 1: 1 molar mixture of  $\text{Eu}_2\text{O}_3$  and  $\alpha\text{-Fe}_2\text{O}_3$ ) where an almost single-phased  $\text{EuFeO}_3$  is attained after 40 h of milling compared to 120 h required for the reactants' mixture with  $x = 0.0$  to yield an almost single-phased  $\text{EuCrO}_3$ . This, we attribute to the lower lattice energy of  $\alpha\text{-Fe}_2\text{O}_3$  ( $-14309 \text{ kJ mol}^{-1}$ ) relative to that of  $\text{Cr}_2\text{O}_3$  ( $-15276 \text{ kJ mol}^{-1}$ ) [36] which, in turn, implies that the bond breaking of  $\alpha\text{-Fe}_2\text{O}_3$  requires a lesser time than does that of  $\text{Cr}_2\text{O}_3$  under similar milling conditions.

(2) The final sintering temperature of the pre-milled reactants' mixtures at which purely single-phased  $\text{EuCr}_{1-x}\text{Fe}_x\text{O}_3$  materials form decrease significantly with increasing  $\text{Fe}^{3+}$  content. Figure 4 illustrates this point for the case with  $x = 1.0$  where a final sintering temperature of only  $500^\circ\text{C}$  was sufficient to yield single-phased  $\text{EuFeO}_3$ . Specifically, the final sintering temperatures decreased from  $950^\circ\text{C}$  for the mixture with  $x = 0.0$ , to  $850^\circ\text{C}$  for those with  $x = 0.1, 0.3$  and  $0.5$ , to  $800^\circ\text{C}$  for that with  $x = 0.7$  to  $500^\circ\text{C}$  for the mixtures with  $x = 0.9$  and  $x = 1.0$ .

As typical example of the size and morphology of the resulting  $\text{EuCr}_{1-x}\text{Fe}_x\text{O}_3$  particles, we present in Figure 5 the TEM image of the sample with  $x = 0.1$ . Compared to the other samples, this sample has the least agglomerated particles. Despite the low quality of the image, it is evident that these *nanocrystalline* particles are irregular in shape and range in size between  $\sim 20 \text{ nm}$  and  $\sim 50 \text{ nm}$ . The lattice parameters obtained for the  $\text{EuCr}_{1-x}\text{Fe}_x\text{O}_3$  nanocrystalline particles are given in Table 1 together with those of the bulk  $\text{EuCrO}_3$  and  $\text{EuFeO}_3$  [29]. The obtained unweighted  $R_p$ , weighted profile  $R_{wp}$ , and expected  $R_{exp}$  factors are in the range (19.23-23.38)%, (29.12-32.60)%, and (0.62-0.77), respectively. Table 1 shows that while the lattice parameters slightly increase with  $x$ , the increase of the  $b$  lattice parameter relative to  $a$  and  $c$  is more pronounced at higher  $x$  values. This expansion of the unit cell with increasing  $x$  is apparently related to the replacement of the smaller  $\text{Cr}^{3+}$  ion ( $0.755\text{\AA}$ ) by the slightly larger high spin  $\text{Fe}^{3+}$  ion ( $0.785\text{\AA}$ ) [37]. The  $b$  lattice parameters of the  $\text{EuCrO}_3$  and  $\text{EuFeO}_3$  nanocrystalline particles are smaller than those of their corresponding bulk [38]. While data for the bulk counterparts of the remaining nanoparticles is lacking, we may conclude that the unit cells of the end members of  $\text{EuCr}_{1-x}\text{Fe}_x\text{O}_3$  nanoparticles are contracted relative to those of their corresponding bulk which could be linked to surface-strain effects such as the Laplace pressure that results from the surface tension [39]. In [25] we have shown that the values of the lattice parameters for all  $\text{EuCr}_{1-x}\text{Fe}_x\text{O}_3$  nanoparticles are related such that:  $a < c/\sqrt{2} < b$ . Taken together, these results

imply that both the reduction of the particle size to the nanometer scale and the presence of  $\text{Cr}^{3+}$  and  $\text{Fe}^{3+}$  ions in the structure lead to crystalline lattice distortion different from that in the bulk counterparts. This distortion is obviously different from the Jahn–Teller distortion according to which the perovskite unit cell parameters are related according to  $c/\sqrt{2} < a < b$  [15,40-43]. Ignoring effects such as strain, which may possibly exist particularly in the samples annealed at relatively low temperatures, and considering the broadening of the XRD reflection peaks to be a consequence of size effects (large surface to volume ratio) and/or the presence of defects that could tilt the lattice and change the lattice parameter, the average crystallite size " $d_{hkl}$ " was determined using the Scherrer formula, viz.:

$$d_{hkl} = \frac{R \lambda}{\beta \cos \theta} \quad (1)$$

where the constant  $R$  is a shape factor ( taken to be 0.90),  $\lambda$  is the wavelength of the X-ray,  $\beta$  is the FWHM corrected for instrumental broadening (by subtracting the FWHM of a standard sample from the actually measured FWHM) and  $\theta$  is the Bragg angle [32,33]. Figure 6 shows that the *average* crystallite size of the  $\text{EuCr}_{1-x}\text{Fe}_x\text{O}_3$  nanoparticles, estimated using the non-overlapping (110) and (111) peaks at  $2\theta$  values of  $\sim 23^\circ$  and  $\sim 26^\circ$  respectively, clearly decreases with increasing  $\text{Fe}^{3+}$  content ( $x$ ). This may be attributed to a possible weakening of the  $\text{Eu}^{3+}\text{-O}^{2-}$  and/or  $\text{Cr}^{3+}\text{-O}^{2-}$  bonds following the substitution of the  $\text{Cr}^{3+}$  ions by the larger  $\text{Fe}^{3+}$  ones in the perovskite structure, making long-range cohesion increasingly difficult. In the present context we have used “crystallite” to mean a “crystalline domain” within a particle. The obtained crystallite sizes’ (Figure 6) combined with the TEM result (Figure 5) are suggestive that the individual nanoparticles are composed of single or few crystallites.

A final comment here is that it could be shown that while for  $x = 0.0$ , the crystallite size of the perovskite  $\text{EuCr}_{1-x}\text{Fe}_x\text{O}_3$  nanoparticles increases as a function of the sintering temperature of the pre-milled mixture until a single-phased  $\text{EuCrO}_3$  sample was attained, for the sample with  $x = 1.0$ ,  $\text{EuFeO}_3$ , no such correlation is observed. Also while the final sintering temperature to get single-phased  $\text{EuCr}_{1-x}\text{Fe}_x\text{O}_3$  samples with  $x = 0.1, 0.3$  and  $0.5$  is the same, the decrease in their average crystallite size as a function of  $x$  (Figure 6) has roughly the same slope as that for the samples with higher  $x$  values. All this suggests that for  $x \geq 0.1$  the sintering temperature is *not* the decisive factor in determining crystallite size.

### 3.2: Magnetism of the $\text{EuCr}_{1-x}\text{Fe}_x\text{O}_3$ nanoparticles:

The temperature variation of the magnetization of the  $\text{EuCr}_{1-x}\text{Fe}_x\text{O}_3$  nanoparticles recorded, in the range 300 – 900 K, with the Faraday balance under a magnetic field of 1.5 T is shown in Figure 7. The inset of Figure 7 shows the temperature dependence of the magnetization curves of the nanoparticles with  $x \leq 0.7$  recorded using the VSM under a magnetic field of 1.35 T in the temperature range 100 – 840 K. It is clear that the room temperature values of magnetic moment per formula unit, measured under a field of 1.5 T, increase almost monotonically from 0.016 to 0.022  $\mu_B$  as  $x$  varies from 0.0 to 1.0. The fact that these values are reasonably smaller than the low temperature value of 0.07  $\mu_B$  reported for bulk  $\text{EuFeO}_3$  [4] could be ascribed to the incomplete antiferromagnetic compensation within the  $\text{Fe}^{3+}/\text{Cr}^{3+}$  sublattice when the moments are tilted by a few degree from the antiferromagnetic axis [13,14] or to surface effects in the nanoparticles.

Generally the magnetization curve  $M(T)$  for each sample can be resolved into two components; namely a weak ferromagnetic component  $M_F(T)$ , and a paramagnetic one,  $M_p(T)$ . Reiterating,  $M_F(T)$  results from the spin canting associated with the asymmetry in the magnetic unit cell, which is an abruptly decaying function of temperature. It follows from the data shown in Figure 7 that the  $\text{EuCr}_{1-x}\text{Fe}_x\text{O}_3$  nanoparticles show a weak ferromagnetic behavior below Curie temperatures ( $T_C$ ) that increase from of 180 K for  $x = 0.0$  to 595 K for  $x = 1.0$  as shown in Table 1. The fact that these values of  $T_C$  are lower than those of the corresponding bulk samples [16], could be attributed to a different distribution of magnetic cations at both A- and B-crystallographic sites as we have proposed in [8] and will also explore using  $^{151}\text{Eu}$  Mössbauer spectra in the next section, and/or particle size effect as has been demonstrated for other nanoparticles with canted antiferromagnetism [44]. It is interesting to observe how the sample with  $x = 0.5$  exhibits the smallest change in the net magnetization as it transits from the paramagnetic to the canted antiferromagnetic state relative to the other  $\text{EuCr}_{1-x}\text{Fe}_x\text{O}_3$  nanoparticles (inset of Figure 7). This, unlike in the case of the  $\text{Cr}^{3+}$ - or  $\text{Fe}^{3+}$ -rich samples, could reflect a disordered distribution of the equal-numbered  $\text{Cr}^{3+}$  and  $\text{Fe}^{3+}$  ions in the perovskite structure that could lead to an almost collinear magnetic ordering. However, the very weakly increasing moment below this transition implies that the antiferromagnetic state is not a pure one.

To investigate the paramagnetic behavior of the  $\text{EuCr}_{1-x}\text{Fe}_x\text{O}_3$  nanoparticles, we have used the magnetization of Figure 7, measured with both the Faraday balance and the VSM, to determine temperature variation of the molar magnetic susceptibility. Noting from Figure 8 that for all values of  $x$ , the *inverse (total) molar magnetic susceptibility* varies

almost *linearly* with temperature above the Curie temperatures ( $T_C$ ), we were tempted to try a careful fit of the variation of the magnetic susceptibility with temperature, in paramagnetic phase, assuming Curie-Weiss (CW) law behavior, namely:

$$\chi(T) = \frac{(N_A \mu_{eff}^2)}{3k_B (T - T_W)} \quad (2)$$

where  $\mu_{eff}$ ,  $k_B$  and  $T_W$  stand for the effective magnetic moment, Boltzmann constant and paramagnetic Curie Weiss temperature, respectively. The resulting  $\mu_{eff}$  and  $T_W$  values are plotted as a function of iron content  $x$  in Figures 9 (a) and (b), respectively. An inspection of Figure 9 shows the effective magnetic moment  $\mu_{eff}$ , except for the samples with  $x = 0.1$  and  $0.9$ , to generally increase with increasing the Fe concentration ( $x$ ). Such a rough correlation between  $\mu_{eff}$  and  $x$  simply reflects the higher magnetic moment of  $Fe^{3+}$  compared to that of  $Cr^{3+}$  and, possibly, reflects a partially disordered distribution of equal-numbered  $Cr^{3+}$  and  $Fe^{3+}$  ions in the perovskite-related structure. Hence, the  $Cr^{3+}$  magnetic moments appear to play a secondary role in modulating the contribution of the  $Fe^{3+}$  ions. The amplitude of  $Cr^{3+}$  modulation is obviously smaller than the contribution of  $Fe^{3+}$ . Due to the high level of structural disorder in these mechanosynthesized nanoparticles it is hard to envisage how strictly parallel or antiparallel the arrangements of the magnetic moments are.

Clearly the two outlying points on the curve of  $\mu_{eff}$  vs.  $x$ , viz. at  $x = 0.1$  and  $0.9$  suggest that a factor other than  $x$  does influence the average moment. Apparently the most plausible of such factors is indeed the disordered magnetic cation distribution. This may not be simply a disorder on the B-site between the  $Cr^{3+}$  and  $Fe^{3+}$  ions, but rather a disorder between A- and B-site cations. In that case the A-site  $Cr^{3+}$  and  $Fe^{3+}$  ions may well have paramagnetic moments that are different from their respective moments on their regular B-sites. As it will be discussed below, such antisite disorder indeed appears to be present in these  $EuCr_{1-x}Fe_xO_3$  nanoparticles. At the same time, the magnetic ions at the surface layers of nanoparticles may also have net magnetic moments that are different from the bulk value, due to a mechanically induced non-equilibrium cation distribution and/or canted spin configuration. However, in the present case, considering the size of the particles one expects such surface effects to have only a minor contribution to the variation of  $\mu_{eff}$  (Fig. 9a), which furthermore should vary with  $x$  in a monotonous manner similar to the particle size. Nevertheless, the considerable drop in the crystallite size while going from  $x = 0.0$  to  $0.1$  (Fig. 6) may also contribute to the corresponding drop of  $\mu_{eff}$  (Fig. 9a). The values of  $\mu_{eff}$  vary between  $5.2$  and  $6.3 \mu_B$ , in agreement with the values expected for transition metal ions [45]. The values of  $T_W$ , which express the mean interaction among magnetic moments, are

found to lie between -290 K and -460 K reflecting the strong antiferromagnetic nature of the nanoparticles [46].

In the preceding analysis, the possible contribution to the molar magnetic susceptibility of the europium ions, expected in the van Vleck formalism [47], was overlooked. As will be shown in the next section,  $^{151}\text{Eu}$  Mössbauer spectroscopy excludes the presence of any diamagnetic  $\text{Eu}^{2+}$  ions in the  $\text{EuCr}_{1-x}\text{Fe}_x\text{O}_3$  nanoparticles, leaving us with two possibilities to consider about the distribution of the  $\text{Eu}^{3+}$  ions within the magnetic lattice. These are whether the  $\text{Eu}^{3+}$  and  $\text{Cr}^{3+}/\text{Fe}^{3+}$  ions compose separate sublattices, as is the case in bulk samples, or do they partially exchange sites over the whole lattice. We will test the first possibility which involves two separate components of the paramagnetic susceptibility, rather than one *total* paramagnetic susceptibility as we have assumed above, originating from the separate  $\text{Eu}^{3+}$  and  $\text{Cr}^{3+}/\text{Fe}^{3+}$  sublattices. The electronic configuration for the  $\text{Eu}^{+3}$  ion,  $[\text{Xe}]4f^6$ , indicates that the lowest energy level multiplet consists of the ground state  $^7\text{F}_0$ , and six excited states  $^7\text{F}_J$  ( $J=1,2,\dots,6$ ).  $\text{Eu}^{+3}$  has 6 f-electrons and the Hund rules give a spin quantum number  $S=3$  and an angular momentum quantum number  $L=3$  for this lowest multiplet. In the Russell-Saunders coupling scheme, the energy levels are formed by the spin-orbit interaction  $\lambda\mathbf{L}\cdot\mathbf{S}$ , where  $\lambda$  is the coupling constant [47]. The difference between successive energy levels is given by  $E_J-E_{J-1}=\lambda J$  (where  $J$  is the total angular momentum number) [45,47]. The non-degenerate (non-magnetic), ground state  $^7\text{F}_0$  and the low lying excited states  $^7\text{F}_J$  are so close that the energy intervals are comparable to thermal energy at room temperature ( $k_B T$ ) [47,48]. According to the van Vleck theory this gives rise to a temperature-dependent contribution to the paramagnetic susceptibility in the high temperature region and a temperature-independent contribution ( $\chi_{TIP}$ ) in the low temperature region depending on the value of  $\lambda$  [47,48]. We have, therefore, re-analyzed the temperature-dependent paramagnetic behavior of the  $\text{EuCr}_{1-x}\text{Fe}_x\text{O}_3$  nanoparticles by treating their paramagnetic molar susceptibility as a sum of the CW-type contribution due to the  $\text{Cr}^{3+}/\text{Fe}^{3+}$  ions,  $\chi(\text{Cr}^{3+}/\text{Fe}^{3+})$ , the van Vleck-type of contribution of  $\text{Eu}^{3+}$ ,  $\chi(\text{Eu}^{3+})$  and the temperature-independent contribution ( $\chi_{TIP}$ ), such that:

$$\chi(T) = \chi(\text{Cr}^{3+}/\text{Fe}^{3+}) + \chi(\text{Eu}^{3+}) + \chi_{TIP} \quad (3)$$

Assuming a coupling constant ( $\lambda$ ) value of  $370 \text{ cm}^{-1}$  (corresponding to 532 K), as was used for  $\text{EuZrO}_3$  [48], it can be shown following Takikawa et al [47] that in the temperature range of our measurements ( $\chi_{TIP}$ ) can be neglected. Hence in our analysis we used:

$$\chi(T) = \chi(\text{Cr}^{3+}/\text{Fe}^{3+}) + \chi(\text{Eu}^{3+}) \quad (4)$$

If we limit ourselves to the first three excited states, the van Vleck magnetic susceptibility of  $\chi(\text{Eu}^{3+})$ , as has been given elsewhere [45,48,49], we have:

$$\chi(\text{Eu}^{3+}) = \frac{N_A \mu_B^2}{3k_B T} \times \frac{24/a + (13.5 - 1.5/a)e^{-a} + (67.5 - 2.5/a)e^{-3a} + (189 - 3.5/a)e^{-6a}}{1 + 3e^{-a} + 5e^{-3a} + 7e^{-6a}} \quad (5)$$

with  $a = \lambda/k_B T$  and  $\mu_B$  being the Bohr magneton. We have assumed the van Vleck susceptibility  $\chi(\text{Eu}^{3+})$  to be the same for all  $\text{EuCr}_{1-x}\text{Fe}_x\text{O}_3$  nanoparticles and used equation (5) to calculate it with the value of  $\lambda$  taken as above. Then the CW-type component of the susceptibility,  $\chi(\text{Cr}^{3+}/\text{Fe}^{3+})$ , was obtained with aid of equation (4) by subtracting  $\chi(\text{Eu}^{3+})$  from the total (measured) paramagnetic susceptibility  $\chi(T)$ . Subsequently, the linear sections in plots of *inverse* susceptibility component of  $\chi(\text{Cr}^{3+}/\text{Fe}^{3+})$  vs. temperature, shown in Figure 10, were fitted to Curie–Weiss law resulting in values of  $\mu_{eff}$  and  $T_W$  per ( $\text{Fe}^{3+}/\text{Cr}^{3+}$ ) ion plotted as a function of iron content  $x$  in Figures 11(a) and (b) respectively. Generally, one notes that the correlation factor for the fitting in Figure 11 is remarkably lower compared to that in Figure 9 inferred on the basis of the Curie-Weiss fitting of the measured inverse “total” susceptibility.

The results summarized in Figure 11 are evidently questionable and hard to explain. For example,  $\mu_{eff}$  is surprisingly found to be very weakly dependent on iron content ( $x$ ) as it changes from 0.0 to 0.5. It is worth noticing that for  $x = 0.9$ ,  $\mu_{eff}$  attains the value  $7.2 \mu_B$  that appreciably exceeds the characteristic value of  $5.9 \mu_B \text{ Fe}^{3+}$  [45]. Additionally,  $T_W$  for the  $\text{EuCrO}_3$  nanoparticles is found to be  $-898 \text{ K}$ , which reveals an unexpectedly strong antiferromagnetic interaction. Moreover for a system with  $x = 0.9$   $T_W$  unrealistically exceeds  $-3160 \text{ K}$ . These results strongly suggest that the assumption that the  $\text{Eu}^{3+}$  and  $\text{Fe}^{3+}/\text{Cr}^{3+}$  ions have separate non-interacting sublattices appears to be too rough an approximation. This again implies, among other options, the possibility of the presence of antisite defects where the  $\text{Eu}^{3+}$ -and  $\text{Cr}^{3+}/\text{Fe}^{3+}$  cations exchanges their crystallographic (magnetic) sites as we proposed in [8,25] and will investigate further in the next section.

### 3.3: Mössbauer spectroscopy

Having previously shown both XRD Rietveld analysis and a careful  $^{151}\text{Eu}$  Mössbauer spectral fit to yield *identical* results about the cationic distribution over the A- and B- sites in  $\text{EuCrO}_3$  nanoparticles [8], we shall only use  $^{151}\text{Eu}$  Mössbauer spectroscopy to explore the cationic distribution within the nanoparticles. Figure 12 shows the  $298 \text{ K}$   $^{151}\text{Eu}$  Mössbauer spectra of the various  $\text{EuCr}_{1-x}\text{Fe}_x\text{O}_3$  samples. The spectra display a broad

absorption peak positioned in the velocity range of 0.6-0.8 mm/s, which confirms that europium is present exclusively in the  $\text{Eu}^{3+}$  oxidation state in these compounds. The  $^{151}\text{Eu}$  Mössbauer spectra of orthochromites and orthoferrites are well known to reflect the presence of a non-zero electric quadrupole interaction at the site of the  $^{151}\text{Eu}$  nucleus [8,10,16,50]. In addition, in the magnetically ordered state of orthoferrites, the Eu nuclei may experience a supertransferred hyperfine magnetic field produced by a magnetic exchange interaction between  $\text{Eu}^{3+}$  ions (having low-lying excited magnetic states being mixed with the non-magnetic  $^7\text{F}_0$  ground state [47,48,51]) and the magnetically ordered 3d ions on neighboring lattice sites [16]. This effect can be based on a partial electron transfer between the  $\text{Eu}^{3+}$  ion and the 3d levels of magnetic ions resulting in an uncompensated spin density at the Eu nuclear site and an associated hyperfine magnetic field [52,53]. As in  $\text{EuFeO}_3$  B-site  $\text{Fe}^{3+}$  spins order antiferromagnetically with only a slight canting leading to the observed weak ferromagnetism, the uncompensated hyperfine magnetic field at the  $\text{Eu}^{3+}$  nucleus is small ( $\sim 1.9$  T as estimated by Gibb [10]), and may be around or below the usual detection limits of  $^{151}\text{Eu}$  Mössbauer spectroscopy. Somewhat larger fields, however, are to be expected when one or more of the 8 nearest-neighbor  $\text{Fe}^{3+}$  ions of A-site  $\text{Eu}^{3+}$  is/are replaced by another type of ion such as  $\text{Cr}^{3+}$  or  $\text{Co}^{3+}$ ; namely, in such a case the mutual compensation of the supertransferred hyperfine magnetic field at  $\text{Eu}^{3+}$  site due to antiferromagnetically aligned B-site ion pairs remains incomplete, giving rise to a larger residual field [16,51].

The preparation method of mechanical milling applied in the present case is known to be a non-equilibrium technique (see, e.g., [21-25,54]) that, together with low-temperature sintering, may lead to a cationic distribution that is unattainable via the conventional high temperature synthesis route. In the present case, the analysis of  $^{151}\text{Eu}$  Mössbauer spectra could, therefore, get further complicated by the possibility of a fractional site exchange between  $\text{Eu}^{3+}$  and the cations that usually occupy the B-site (*viz.*  $\text{Fe}^{3+}$  and  $\text{Cr}^{3+}$ ) as we have shown for mechanosynthesized  $\text{EuCrO}_3$  nanoparticles [8].

As the  $^{151}\text{Eu}$  Mössbauer spectra of  $\text{EuCr}_{1-x}\text{Fe}_x\text{O}_3$  (Figure 12) refer to the presence of nonzero hyperfine interaction(s), a formal fit to a single Lorentzian similar to that used for high-temperature synthesized bulk samples [16], may reveal – through the peak's FWHM width – the appearance of a nonzero supertransferred hyperfine field at the  $\text{Eu}^{3+}$  nuclei developing due to the  $\text{Cr}^{3+} \rightarrow \text{Fe}^{3+}$  substitution. Figure 13 shows the peak widths thus obtained for the present nanoparticles along with corresponding bulk data – taken from [16]. The overall larger peak width observed for the present samples is in part due to the samples'

larger surface density used in the present experiments (35 mg/cm<sup>2</sup> versus 20 mg/cm<sup>2</sup> in reference [16]). However, at lower Cr<sup>3+</sup> concentrations ( $x \geq 0.9$ ) we observe anomalously large peak widths that are apparently *not* accountable for by the random distribution of Cr<sup>3+</sup> ions at B sites as proposed by Gibb for the variation of peak width in the case of the bulk samples (Figure 13) [16]. In addition, the difference between the peak widths observed for EuCrO<sub>3</sub> and EuCr<sub>1-x</sub>Fe<sub>x</sub>O<sub>3</sub> with  $x = 0.1-0.5$  is more pronounced in the present case.

Beside the fit with a single Lorentzian, several further attempts have been made to fit the <sup>151</sup>Eu Mössbauer spectra shown in Figure 12. In all cases the background level was approximated by a third order polynomial to account properly for the apparent nonlinear baseline in the spectra. In the various fits each individual spectral component was fitted by the solution of the static Hamiltonian [55] that takes into account all the 48 transitions generally possible between the excited ( $I_e = 7/2$ ) and ground ( $I_g = 5/2$ ) states of the <sup>151</sup>Eu nucleus when combined electric quadrupole and hyperfine magnetic interactions are present. On the basis of magnetic measurements (Figure 7), for the nanoparticles with  $x = 0, 0.1$  and  $0.3$  we have assumed zero hyperfine magnetic field at the <sup>151</sup>Eu nuclei, whereas for the samples with higher Fe<sup>3+</sup> concentration ( $x$ ) the hyperfine magnetic field was allowed to vary during the fits. An independent fit assuming Eu<sup>3+</sup> to be located only at the A-sites provided unreasonable results with internal line widths varying between 2.4 mm/s and 3.5 mm/s, and with the main component of the electric field gradient,  $V_{zz}$ , varying inconsistently as a function of  $x$ . This indicates that reliable analysis of the spectra is possible only by applying appropriate and physically reasonable constraints on the fit parameters. In the fit model leading to the results presented below we have adopted the following constraints.

(1) As an attempt to account for the possible presence of Eu<sup>3+</sup> ions on both (A and B) sites, all the spectra were decomposed into two subcomponents whose internal line widths were restricted to be the same. The  $V_{zz}$  value characteristic to Eu<sup>3+</sup> ions on the octahedral B sites was restricted to be  $2^{3/2} \approx 2.83$  times of that characteristic to Eu ions on A-sites, in accordance with our recent finding [8] that in EuCrO<sub>3</sub> the ratio of the main component of the electric field gradient characteristic to Eu<sup>3+</sup> ions on A- and B-sites appears to reflect the ratio ( $2^{1/2}$ ) of the corresponding average Eu-O distances. The asymmetry parameter characterizing the electric field gradient tensor (EFG) at the nucleus of B-site Eu<sup>3+</sup> ions,  $\eta_B$ , was furthermore assumed to be the same for all values of  $x$ . Though the latter constrain is inevitably a rough approximation, due to the rather

minor effect  $\eta_B$  exerts on the overall fit model curve, its value could not be determined reliably independently for the different compounds.

(2) Instead of determining the  $^{151}\text{Eu}$  isomer shift of B-site  $\text{Eu}^{3+}$  ions independently in all of the compounds (which did not appear to be feasible), we aimed only at the determination of a characteristic difference ( $\delta_+$ ) between the  $^{151}\text{Eu}$  isomer shifts of A- and B-site  $\text{Eu}^{3+}$  ions. Accordingly, the  $^{151}\text{Eu}$  isomer shift of the B-site  $\text{Eu}^{3+}$  ions ( $\delta_B$ ) was assumed to be expressible as  $\delta_B = \delta_A + \delta_+$ , where  $\delta_A$  denotes the  $^{151}\text{Eu}$  isomer shift of A-site  $\text{Eu}^{3+}$  ions and  $\delta_+$  is a fit parameter that was assumed to be the same for all the studied compounds.

(3) The internal linewidth was assumed to be the same for all the fitted components in all the spectra due to the identical sample surface density ( $35 \text{ mg/cm}^2$ ).

(4) The main component of the EFG tensor ( $V_{zz}$ ) characteristic to A-site  $\text{Eu}^{3+}$  ions was assumed to be independent of the  $\text{Fe}^{3+}$  concentration ( $x$ ). This is based on the finding that  $V_{zz}$  in  $\text{EuCrO}_3$  and in  $\text{EuFeO}_3$  at room temperature agree within the experimental error [34].

(5) The polar and azimuthal angles of the direction of the hyperfine magnetic field (measured with respect to the eigensystem of the EFG tensor) at the  $^{151}\text{Eu}$  nuclei was assumed to be independent of the  $x$  iron concentration.

On the basis of the above constraints simultaneous two-site fitting of the  $^{151}\text{Eu}$  spectra of the  $\text{EuCr}_{1-x}\text{Fe}_x\text{O}_3$  samples provided the following reasonable results. The angle enclosed between the direction of the hyperfine magnetic field and the  $z$  axis of the eigensystem of the EFG (i.e. the  $\beta$  polar angle) was found to be  $\sim 93^\circ$  (4) and  $\sim 90^\circ$  (13) for the A and B sites, respectively. These values, that may be taken as  $90^\circ$  within the experimental error, are in agreement with the established magnetic structure of  $\text{EuFeO}_3$  [10,51], implying that the  $\text{Fe}^{3+}$  magnetic moments are aligned antiferromagnetically along the crystallographic  $a$  axis, but at the same time being slightly canted yielding an effective magnetization along the crystallographic  $c$  axis which is perpendicular to the direction of the  $z$  axis of the eigensystem of the EFG as the latter axis lies on the  $ab$  plane. For the azimuthal angle  $\alpha$ , the fit gave  $0^\circ$  for both sites (though error estimation based on Monte Carlo techniques indicated that statistically the obtained  $\alpha$  values may be poorly defined for the B sites), indicating that the smallest component of the EFG,  $V_{xx}$ , is measured along the direction of the hyperfine magnetic field, i.e. along the  $c$  axis. While this orientation satisfies the criterion – put forward by Gibb [10] on the basis of symmetry considerations –

that in  $\text{EuFeO}_3$  one of the principal axes of the EFG at  $\text{Eu}^{3+}$  nuclei must be along the  $c$  axis, it is in contrast with Gibb's prediction that in  $\text{EuFeO}_3$  the second largest component of the EFG,  $V_{yy}$ , should be measured along the  $c$  axis [10]. Nevertheless, as the observed values of  $\alpha$  and  $\beta$  correspond well with basic requirements concerning the structure of  $\text{EuFeO}_3$ , we have taken  $\alpha = 0^\circ$  and  $\beta = 90^\circ$  as their precise values, and repeated the simultaneous fit of the  $^{151}\text{Eu}$  spectra by fixing these angles' values for both sites so as to deduce more precise values for the remaining parameters. The results of this latter fit are discussed below.

The common internal linewidth of the spectral components was found to be 1.86(4) mm/s. For the main component of the EFG tensor  $V_{zz,A} = -5.0(1) \times 10^{21} \text{ V/m}^2$  ( $eQ_g V_{zz,A} \approx -6.32(15) \text{ mm/s}$ ) and  $V_{zz,B} = -14.2(3) \times 10^{21} \text{ V/m}^2$  ( $eQ_g V_{zz,B} \approx -17.9(4) \text{ mm/s}$ ) were obtained for  $\text{Eu}^{3+}$  on A- and B-sites, respectively. These values are somewhat higher than the corresponding distribution averages we found concerning  $\text{EuCrO}_3$  [8], but  $eQ_g V_{zz,A}$  agrees well with the corresponding values  $-6.09(30) \text{ mm/s}$  [50] and  $\sim -6.5 \text{ mm/s}$  [10] reported earlier for A-site  $\text{Eu}^{3+}$  in  $\text{EuFeO}_3$ . Clearly the asymmetry parameter ( $\eta_A$ ) characteristic to the EFG at the nucleus of  $\text{Eu}^{3+}$  ions at the A-site, given in Table 2 as a function of  $\text{Fe}^{3+}$  concentration ( $x$ ) tends to be larger (0.6 – 0.8) at higher ( $x \geq 0.5$ ) iron concentrations, in accordance with earlier results showing that  $\eta_A$  is higher in  $\text{EuFeO}_3$  than in  $\text{EuCrO}_3$  [49]. The common value of the asymmetry parameter obtained for the component attributed to B-site  $\text{Eu}^{3+}$  ions turned out to be 0.80(5).

The obtained values of the  $^{151}\text{Eu}$  isomer shift for A-site  $\text{Eu}^{3+}$  ions ( $\delta_A$ ), given in Table 2 as a function of the  $\text{Fe}^{3+}$  concentration ( $x$ ), are in good agreement with earlier results for A-site  $\text{Eu}^{3+}$  in  $\text{EuCrO}_3$  (0.68(4) mm/s) and  $\text{EuFeO}_3$  (0.72(6) mm/s) [50]. The tendency of  $\delta_A$  to increase with  $x$  may reflect an electron density transfer between  $\text{Eu}^{3+}$  and  $\text{Fe}^{3+}$ , in agreement with the Eu-Fe magnetic exchange interaction and the associated supertransferred hyperfine magnetic field [16,51] hypothesized to be present in this system. The common (i.e. independent of  $x$ ) deviation assumed to exist between  $\delta_A$  and  $\delta_B$  was found to be  $\delta_+ = \delta_B - \delta_A = +0.06(3) \text{ mm/s}$ , suggesting a larger electron density transfer between  $\text{Eu}^{3+}$  and  $\text{Fe}^{3+}/\text{Cr}^{3+}$  when  $\text{Eu}^{3+}$  is positioned at the B-site, which in turn would be expected to result in a larger supertransferred hyperfine magnetic field for B-site  $\text{Eu}^{3+}$  ions.

The  $^{151}\text{Eu}$  hyperfine magnetic field data obtained, shown in Figure 14, is consistent with the above-mentioned expectation. Specifically for the nanoparticles with  $x = 0.5$  the effective hyperfine magnetic field displayed by the B-site component was found to be significantly higher than that displayed by the component associated with A-site  $\text{Eu}^{3+}$  ions.

The corresponding numerical values are listed in Table 2. The hyperfine magnetic field characteristic to A-site  $\text{Eu}^{3+}$  ions increases with  $x$  for  $x \geq 0.5$ , without displaying the decrease expected for  $\text{EuFeO}_3$  as predicted by Gibb [16] on the basis that in pure  $\text{EuFeO}_3$  the effective exchange interaction between  $\text{Eu}^{3+}$  and the neighboring  $\text{Fe}^{3+}$  ions would be largely suppressed by having the four pairs of nearest-neighbor antiferromagnetically-aligned  $\text{Fe}^{3+}$  ions cancelling each other's effect. This finding is in agreement with our hypothesis that the present  $\text{EuCr}_{1-x}\text{Fe}_x\text{O}_3$  nanoparticles display cationic site disorder, with a considerable amount of  $\text{Eu}^{3+}$  cations being located at the B-sites. Namely, B-site  $\text{Eu}^{3+}$  ions would maintain an imbalance in the exchange interaction on neighboring A-site  $\text{Eu}^{3+}$  ions even if the concentration of substituent Cr ions is not sufficient to achieve the same effect. This is also in agreement with the lack of downturn of the single Lorentzian peak width (Figure 13) associated with the sample of  $x = 1.0$ , though the corresponding large apparent peak width should be contributed to also by the larger hyperfine magnetic field found for B-site  $\text{Eu}^{3+}$  ions (Figure 14). The difference between the  $^{151}\text{Eu}$  hyperfine magnetic fields of  $\sim 4.3$  T obtained for  $x = 0.7$  and  $0.9$ , and  $\sim 8.5$  T for  $x = 1.0$  (Table 2) presumably reflects the effect of the number of  $\text{Fe}^{3+}$  ions – being nearest neighbors to B-site  $\text{Eu}^{3+}$  ions – on the supertransferred hyperfine magnetic field at the nucleus of B-site europium.

It remains to note that the present findings corroborate those reported in our previous study on mechanothesized  $\text{EuCrO}_3$  nanoparticles [8] where convincing evidence has been presented concerning the presence of  $\text{Eu}^{3+}$  cations at both the usual A- and unusual B-sites of the perovskite-related  $\text{ABO}_3$  structure. As the nanoparticles investigated in the present work are closely related to those studied there, it is only logical that any reasonable structural model of the  $\text{EuCr}_{1-x}\text{Fe}_x\text{O}_3$  nanoparticles should also include the possibility of the  $\text{Eu}^{3+}$  ions being present at both crystallographic sites. Consequently, a physically reasonable interpretation of the  $^{151}\text{Eu}$  Mössbauer spectra of  $\text{EuCr}_{1-x}\text{Fe}_x\text{O}_3$  nanoparticles should rely on at least two spectral subcomponents to account for the partial occupancy of both A-sites and B-sites by  $\text{Eu}^{3+}$  ions. It is pertinent to show how the findings of present study correlate well with those of our recent  $^{57}\text{Fe}$  Mössbauer study on the same  $\text{EuCr}_{1-x}\text{Fe}_x\text{O}_3$  nanoparticles [25]. In that study, we have shown that recording the  $^{57}\text{Fe}$  Mössbauer spectra of the  $\text{EuCr}_{1-x}\text{Fe}_x\text{O}_3$  nanoparticles at 78 K, a temperature that is well below their Curie temperatures, has resulted in well resolved Zeeman magnetic six-line patterns, each of which was fitted with two sextets. The sextet with the larger spectral area and hyperfine field in the spectrum of each sample was attributed to majority normal B-site  $\text{Fe}^{3+}$  ions having the usual cationic neighborhood, whereas the one with the smaller spectral area and hyperfine field was

associated mostly with  $\text{Fe}^{3+}$  either at A-sites or at B-sites with one or more  $\text{Eu}^{3+}$  and/or  $\text{Cr}^{3+}$  at nearest-neighbor B sites. Figure 15 shows the relative area fraction of the  $^{151}\text{Eu}$  Mössbauer spectrum component attributed to B-site  $\text{Eu}^{3+}$  ions obtained in the present study along with the estimated concentration of  $\text{Fe}^{3+}$  ions associated with the minority component found in the corresponding  $^{57}\text{Fe}$  Mössbauer spectra recorded at 78 K as a function  $x$  [25]. The latter values were calculated by multiplying the  $x$  concentration of iron with the relative area fraction of the minority  $^{57}\text{Fe}$  Mössbauer spectrum component as found at 78 K [25]. Clearly, for  $x \geq 0.5$  there is a remarkable agreement between the estimated concentration of  $\text{Fe}^{3+}$  ions contributing to the minority sextet component in the  $^{57}\text{Fe}$  Mössbauer spectra [25] and the fractions of the B-site  $\text{Eu}^{3+}$  ions inferred from  $^{151}\text{Eu}$  Mössbauer spectroscopy. Given that a smaller exchange field is expected to act on an  $\text{Fe}^{3+}$  ion whose  $\text{Fe}^{3+}$  neighbors are in part replaced by  $\text{Eu}^{3+}$ , this also provides an explanation for the decreased hyperfine magnetic field reflected by the minority  $^{57}\text{Fe}$  Mössbauer spectrum component. For the nanoparticles with  $x=0.3$ , the weight of the minority  $\text{Fe}^{3+}$  spectral component is approximately half of that of the B-site  $\text{Eu}^{3+}$  spectral component (Figure 15). This is understandable given that at low  $\text{Fe}^{3+}$  concentration, the  $\text{Eu}^{3+}$ - $\text{Cr}^{3+}$  cationic site exchange is largely responsible for the cationic site disorder. Generally Figure 15 shows, within experimental errors, that in the  $\text{EuCr}_{1-x}\text{Fe}_x\text{O}_3$  nanoparticles about 15-20 % of the  $\text{Eu}^{3+}$  ions on average exchange their "bulk" normal perovskite sites with  $\text{Cr}^{3+}/\text{Fe}^{3+}$  ions. This could explain why assuming separate magnetic lattices for  $\text{Eu}^{3+}$  and  $\text{Cr}^{3+}/\text{Fe}^{3+}$  in our analysis of the paramagnetic susceptibility led to unreasonable results.

#### 4. Conclusions

Nanocrystalline  $\text{EuCr}_{1-x}\text{Fe}_x\text{O}_3$  particles (20–50 nm) have been prepared successfully via ball milling and subsequent sintering at significantly low temperatures relative to those at which the corresponding bulk samples are usually prepared. It was found that with increasing  $\text{Fe}^{3+}$  concentration the average crystallite size decreases, the lattice parameters increase and the distortion of the orthorhombic unit cell gets more pronounced. Magnetic measurements have shown the particles to be essentially antiferromagnetic with a slight spin canting resulting in weak ferromagnetism. The nanoparticles show a weak ferromagnetism below considerably smaller Curie temperatures ( $T_C$ ) relative to their bulk counterparts. A Curie Weiss fit for the total paramagnetic magnetic susceptibilities gave acceptable values of  $\mu_{eff}$  in the range between 5.2- 6.3  $\mu_B$  and Curie Weiss temperatures,  $T_W$ , in the range

between -300 and -460 K which are suggestive of the strong antiferromagnetism. The assumption that the total paramagnetic magnetic susceptibilities contain van Vleck-type contributions due to  $\text{Eu}^{3+}$  ions, has led to unexpected and inexplicable magnetic moments ( $\mu_{\text{eff}}$ ) and the Curie Weiss temperatures ( $T_{\text{W}}$ ), when the  $\text{Eu}^{3+}$  ions were taken to form a separate lattice relative to the ( $\text{Cr}^{3+}/\text{Fe}^{3+}$ ) one. This was consistent with  $^{151}\text{Eu}$  Mössbauer spectra that indicate the presence of a non-equilibrium cation distribution in the nanoparticles, with a considerable amount of the  $\text{Eu}^{3+}$  and transition metal ( $\text{Cr}^{3+}/\text{Fe}^{3+}$ ) ions exchanging their normal crystallographic sites in the perovskite-related structure. Such an unusual partial cationic site exchange in the nanoparticles is seemingly related to their large surface areas which dominates the contributions made by their tiny bulk cores. The analysis of  $^{151}\text{Eu}$  Mössbauer spectra based on the hypothesis of the  $\text{Eu}^{3+}$ - $\text{Cr}^{3+}/\text{Fe}^{3+}$  site exchange provided interesting results including the Mössbauer parameters characteristic to  $\text{Eu}^{3+}$  ions on the B-sites in  $\text{EuCr}_{1-x}\text{Fe}_x\text{O}_3$ . The supertransferred hyperfine magnetic field at the  $^{151}\text{Eu}$  nuclei was found to be considerably larger for B-site  $\text{Eu}^{3+}$  ions than for  $\text{Eu}^{3+}$  at the A-site. The existence of partial cationic site exchange is supported by the recently reported 78 K  $^{57}\text{Fe}$  Mössbauer data of the  $\text{EuCr}_{1-x}\text{Fe}_x\text{O}_3$  nanoparticles [25] which suggested site occupancies for both sites that remarkably agree with those inferred from their  $^{151}\text{Eu}$  Mössbauer spectra.

#### ***Acknowledgement:***

HMW acknowledges the support of ICTP (Italy) and The Open University (UK) where parts of this article have been written. The continuous support of Intisar Sirour and discussions with Dr. A. I. Arbab are gratefully acknowledged. This work was partly performed within the COST MP903 action supported in part by the Ministry of Science and Higher Education (PL) and WBI (B) in a framework of scientific exchange agreement.

#### **References:**

- [1] X. Niu, W. Du, W. Du, *Sens Actuators B Chem.*, 99 (2004) 399.
- [2] L. Ju, Z. Chen, L. Feng, W. Dong, F. Zheng, M. Shen, *J. Am. Ceram. Soc.*, DOI:10.1111/j.1551-2916.2011.04522.x
- [3] S. Khatiwada, D. Seifu, *Hyperfine Interact.*, 188 (2009) 35.
- [4] K. Tsushima, I. Takemura, S. Osaka, *Solid State Commun.*, 7 (1969) 71.
- [5] G A Smolenskiĭ, E I Golovenchits and V A Sanina, *Sov. Phys. Usp.* 25 (1982) 632.
- [6] M. V. Kuznetsov, I. P. Parkin, *Polyhedron* 17 (1998) 4443.
- [7] E. I. Golovenchits, B. D. Laĭkhtman, V. A. Sanina, *JETP Lett.*, 31 (1980) 223.

- [8] H. M. Widatallah, S. H. Al-Harhi, C. Johnson, Z. Klencsár, A. M. Gismelseed, E. A. Moore, A. D. Al-Rawas, C. I. Wynter, D. E. Brown, *J. Phys. D: Appl. Phys.* 44 (2011) 265403
- [9] S. Geller, *Acta Crystallogr.*, 10 (1957) 243.
- [10] T. C. Gibb, *J. Chem. Soc. Dalton Trans.*, (1981) 2245.
- [11] H. T. Stokes, E. H. Kisi, D. M. Hatch, C. J. Howard, *Acta Crystallographica Section B* 58 (2002) 934
- [12] M. Sivakumar, A. Gedanken, D. Bhattacharya, I. Brukental, Y. Yeshurun, W. Zhong, Y. W. Du, I. Felner, and I. Nowik, *Chem. Mater.* 16 (2004) 3623
- [13] M. Eibschütz, S. Shtrikman, D. Treves, *Phys. Rev.*, 156 (1967) 562.
- [14] H. Xu, X. Hu, L. Zhang, *Cryst. Growth Des.*, 8 (2008) 2061
- [15] L-P. Li, X-Y Song, W- Su, Q. Wei, Z-J. Kang, *Hyperfine Interact.*, 116 (1998) 167
- [16] T. C. Gibb, *J. Chem. Soc. Dalton Trans.*, (1983) 2031.
- [17] L-P. Li, X-M Lin, Q. Wei, X-L., Ren Ren, W-H. Su, *Kao Teng Hsueh Hsiao Hua Heush Hsueh Pao/ Chemical Journal of Chinese Universities*, 19 (1998) 275.
- [18] X. Liu, M. Jin, W. Zha, M. Lu, W. Su, *Hyperfine Interact.*, 68 (1991) 237.
- [19] V. Šepelák, A. Feldhoff, P. Heitjans, F. Krumeich, D. Menzel, F. J. Litterst, I. Bergmann, K. D. Becker, *Chem. Mater.*, 18 (2006) 3057.
- [20] S. Mørup, D.F. Madsen, C. Frandsen, C. R. H. Bahl, M. Hansen, *J. Phys: Condens. Matter*, 19 (2007) 213202.
- [21] H. M. Widatallah, A. D. Al-Rawas, C. Johnson, S. H. Al-Harhi, A.M. Gismelseed, E.A. Moore, S. J. Stewart, *J. Nanosci. Nanotech.* 9 (2009) 2510.
- [22] H. M. Widatallah, C. Johnson, A.M. Gismelseed, I. A. Al-Omari, S.J. Stewart, S.H. Al-Harhi, S. Thomas, , H. Sitepu, *J. Phys. D: Appl. Phys.*, 41 (2008) 165006.
- [23] H. M. Widatallah, I. A. Al-Omari, F. Sives, M. B. Sturla, S. J. Stewart, *J. Mag. Mag. Mater.*, 320 (2008) e326.
- [24] H. M. Widatallah, A. M. Gismelseed, A. A. Yousif, A. D. Al-Rawas, I. A. Al-Omari, S. Al-Tai, M. E. Elzain, C. Johnson, *J. Appl. Phys.*, 97 (2005) 10J306.
- [25] H. M. Widatallah, T. Al Shahumi, A. M. Gismelseed, Z. Klencsár, I. A. Al-Omari, A. D. Al Rawas, M. E. Elzain, A. A. Yousif, *Hyperfine Interact.*, 205 (2012) 101.
- [26] D. Sánchez, J. A. Alonso, M. García-Hernández, M. J. Martínez-Lope, J. L. Martínez, *Phys. Rev. B* 65, J. L. Martinez, *Phys. Rev. B* 65, (2002) 104426.
- [27] Jan-Willem G. Bos, J. Paul Attfield, *Phys. Rev. B* 69, (2004) 094434.

- [28] J. Lian, L. Wang, J. Chen, K. Sun, R. C. Ewing, J. M. Farmer, L. A. Boatne, *Acta Mater.*, 51 (2003) 1493.
- [29] J. Zhang, J. Lian, F. Zhang, J. Wang, A. Fuentes, R. C. Ewing, *J. Phys. Chem.*, C114, (2010) 11810.
- [30] D Serrate, J M De Teresa, M R Ibarra, *J. Phys.: Condens. Matter*,19 (2007) 023201.
- [31] W. Kraus, G. Nolze *J. Appl. Cryst.*, 29 (1996) 301.
- [32] B.D. Cullity, S.R. Stock, *Elements of X-Ray Diffraction*, 3rd Ed., Prentice-Hall Inc., 2001, pp. 167-171.
- [33] R. Jenkins & R.L. Snyder, *Introduction to X-ray Powder Diffractometry*, John Wiley & Sons Inc., 1996, pp. 89-91.
- [34] Z. Klencsár, E. Kuzmann, A. Vértes, *J. Radioanal. Nucl. Chem.*, 210 (1996) 105.
- [35] D. Seifu, L. Takacs, A. Kebede, *J. Mag. Mag. Mater.*, 302 (2006) 479.
- [36] D. R. Lide, *CRC Handbook of Chemistry and Physics*, 87th Edition, CRC Press, Taylor and Francis, Boca Raton, Fl, 2006, pp. 12-24.
- [37] M. J. Winter, [www.webelements.com](http://www.webelements.com).
- [38] M. M. Schieber, *Experimental Magnetochemistry*, John. Wiley and Sons, Inc., and North-Holland Publishing Co., New York and Amsterdam, 1967.
- [39] A.A. Nazorov, R. Mulyukov in *Handbook of Nanoscience, Engineering, and Technology*, W. A. Goddard III, D. W. Brenner, S. E. Lyshevski, and G. J. Iafrate (Eds.), CRC Press, Boca Raton, Fla., 2003, pp.22.1-22.34.
- [40] M. W. Lufaso, P. M. Woodward, *Acta Cryst. B*60, (2004)10.
- [41] P. M. Woodward, *Acta Cryst. B*53, (1997) 32.
- [42] P. M. Woodward, *Acta Cryst. B*53, (1997) 44.
- [43] J. B. Goodenough, *Annu. Rev. Mater. Sci.* 28 (1998) 1.
- [44] D. Wang, M. Gong, *J. Appl. Phys.*, 109 (2011) 114304.
- [45] A.H. Morrish, *The Physical Principles of Magnetism*, Wiley, NY 1965.
- [46] Y. Doi, Y. Hinatsu, *J. Phys. : Condens. Matter*, 11 (1999) 4813.
- [47] Y. Takikawa, A. Ebisu, S. Nagata, *J. Phys. Chem. Solids*, 71 (2010) 1592.
- [48] Y. Zong, K. Fujita, H. Akamatsu, S. Muria, K. Tanaka, *J. Solid State Chem.*, 183 (2010) 168.
- [49] A. Frank, *Phys. Rev.* 39 (1932) 119.
- [50] Z.M. Stadnik, E. de Boer, *Solid State Commun.*, 50 (1984) 335.
- [51] T. C. Gibb, *J. Chem. Soc. Dalton Trans.*, (1983) 873.
- [52] N.L. Huang, R. Orbach, E. Šimánek, J. Owen, D. Taylor, *Phys. Rev.*, 156 (1967) 383.

- [53] A. Vértes, L. Korecz, K. Burger, Mössbauer Spectroscopy. Elsevier, Amsterdam, 1979, p. 91.
- [54] J.Z. Jiang, P. Wynn, S. Mørup, T. Okada, F.J. Berry, NanoStructured Mater., 12 (1999) 737.
- [55] W. Kündig, Nucl. Instr. Meth. 48 (1967) 219.

**Table (1):** The lattice parameters and Curie temperatures ( $T_C$ ) obtained for the  $\text{EuCr}_{1-x}\text{Fe}_x\text{O}_3$  nanocrystalline particles. The values in brackets and italics are for the corresponding bulk [29].

$x$	$a$ (Å)	$b$ (Å)	$c$ (Å)	$T_C$ ( $\pm 4$ K)
0.0	5.3493 (5.340)	5.4936 (5.515)	7.6263 (7.622)	180
0.1	5.3515	5.5050	7.6308	157
0.3	5.3576	5.5221	7.6401	200
0.5	5.3643	5.5417	7.6529	333
0.7	5.3686	5.5583	7.6612	498
0.9	5.3729	5.5847	7.6747	585
1.0	5.3741 (5.370)	5.5821 (5.611)	7.6804 (7.686)	595

**Table (2):** The 298 K  $^{151}\text{Eu}$  Mössbauer parameters for the  $\text{EuCr}_{1-x}\text{Fe}_x\text{O}_3$  samples, obtained via the simultaneous fit of the  $^{151}\text{Eu}$  Mössbauer spectra as described in the text. The given error values refer to the standard deviation of the corresponding parameter value. Values of further fit parameters – that were subject to a constraint during the fit – are given in the text.

$x$	$\delta_A$ ( $\text{mm s}^{-1}$ )	$B_A$ (T)	$\eta_A$	Area fraction of the B-site component (%)	$B_B$ (T)
0.0	0.672(9)	0 (fixed)	0.39(6)	18 $\pm$ 2	0 (fixed)
0.1	0.73(3)	0 (fixed)	0.00(32)	23.7 $\pm$ 4	0 (fixed)
0.3	0.646(14)	0 (fixed)	0.28(13)	23.2 $\pm$ 2	0 (fixed)
0.5	0.711(17)	1.00(13)	0.70(12)	18.3 $\pm$ 3	1.6 $\pm$ 2
0.7	0.777(14)	2.625(62)	0.74(12)	17.3 $\pm$ 2	4.3 $\pm$ 0.4
0.9	0.775(13)	2.628(65)	0.74(10)	15.3 $\pm$ 2	4.3 $\pm$ 0.5
1.0	0.730(14)	2.723(58)	0.62(13)	17.5 $\pm$ 1.5	8.5 $\pm$ 0.3

$\delta_A$ : isomer shift of the  $^{151}\text{Eu}$  on the A-site;  $B_A$  and  $B_B$ : hyperfine magnetic field of the  $^{151}\text{Eu}$  on the A-site and B-site respectively;  $\eta_A$ : the asymmetry parameter of the EFG associated with  $\text{Eu}^{3+}$  ions on the A-sites

**Figures:**

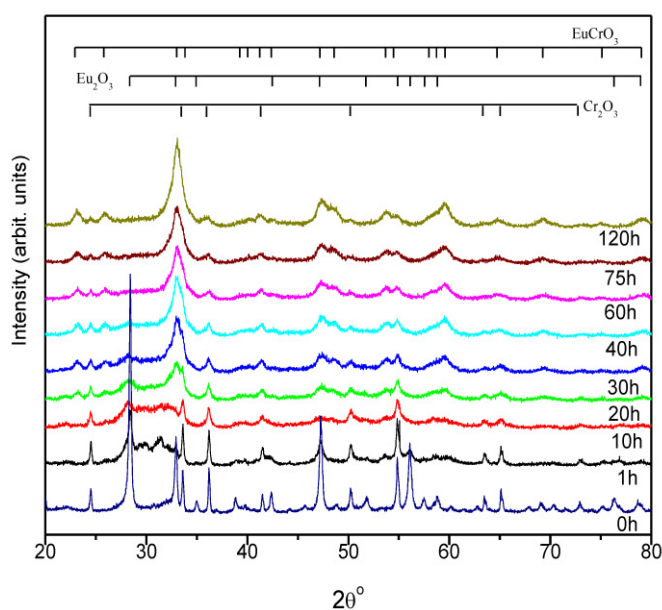


**Figure 1:** The XRD patterns of the 1:1:  $x$  molar mixture of *cubic*  $\text{Eu}_2\text{O}_3$ ,  $\text{Cr}_2\text{O}_3$  and  $\alpha\text{-Fe}_2\text{O}_3$  with  $x = 0.0$  (i.e. 1: 1 molar mixture of *cubic*  $\text{Eu}_2\text{O}_3$  and  $\text{Cr}_2\text{O}_3$ ) milled for the times shown. The bars refer to the positions of the major XRD reflection peaks of the compound indicated. The Miller indices given refer to *monoclinic*  $\text{Eu}_2\text{O}_3$ .

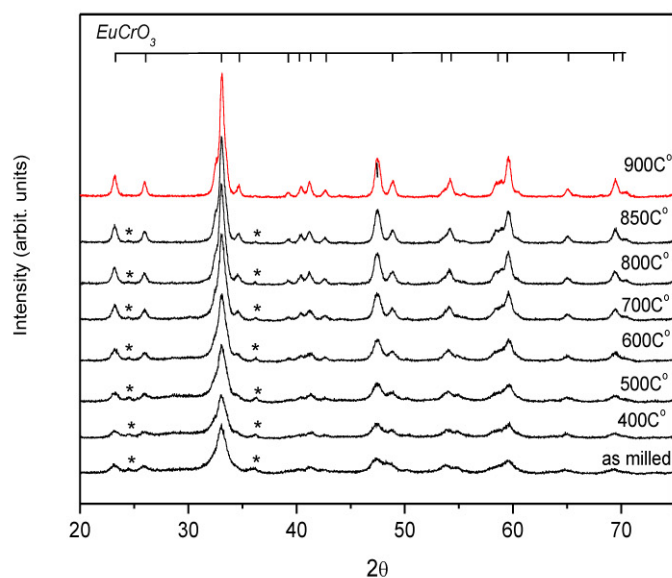


**Figure 2:** The XRD patterns of the 120 h pre-milled the 1:1:  $x$  molar mixture of *cubic*  $\text{Eu}_2\text{O}_3$ ,  $\text{Cr}_2\text{O}_3$  and  $\alpha\text{-Fe}_2\text{O}_3$  with  $x = 0.0$  (1: 1 molar mixture of *cubic*  $\text{Eu}_2\text{O}_3$  and  $\text{Cr}_2\text{O}_3$ ) sintered (8 h) at the temperatures indicated. The symbol (\*) refers to the major peaks of the un-reacted  $\text{Cr}_2\text{O}_3$  that disappear after sintering at  $900^\circ\text{C}$ .

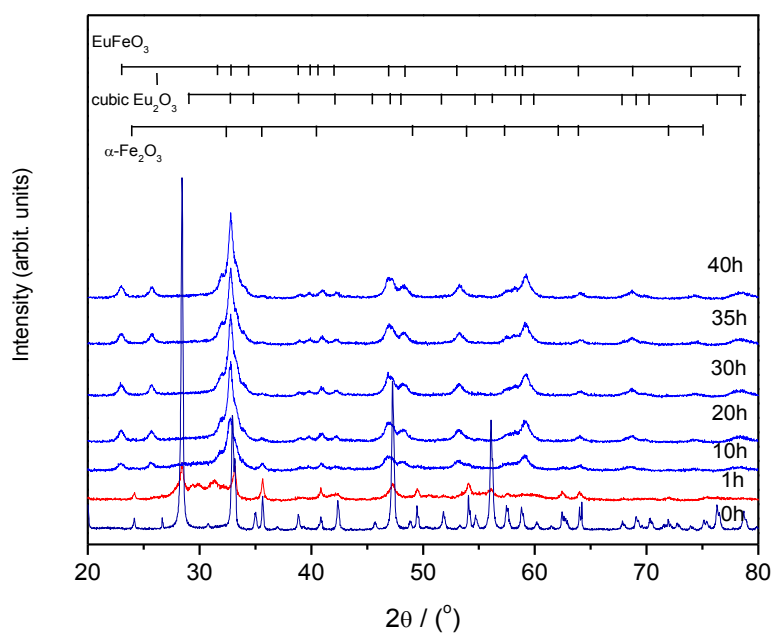


**Figure 3:** The XRD patterns of the 1:0:1 molar mixture of *cubic*  $\text{Eu}_2\text{O}_3$ ,  $\text{Cr}_2\text{O}_3$  and  $\alpha\text{-Fe}_2\text{O}_3$  ( $x = 1.0$ ) milled for the times shown. The bars refer to the positions of the major XRD reflection peaks of the compound indicated.

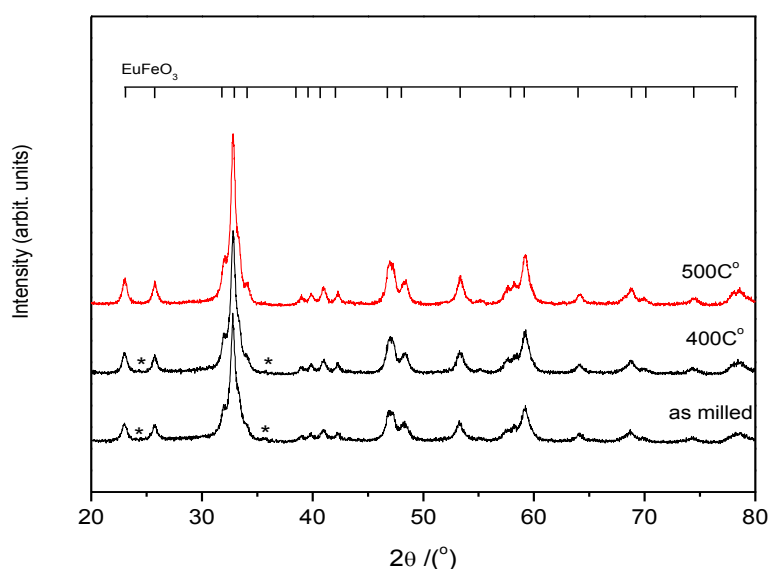


**Figure 4:** The XRD patterns of the 40 h pre-milled 1:0:1 molar mixture of *cubic*  $\text{Eu}_2\text{O}_3$ ,  $\text{Cr}_2\text{O}_3$  and  $\alpha\text{-Fe}_2\text{O}_3$  ( $x = 1.0$ ) after sintering (8 h) at the temperatures indicated. The symbol (\*) refers to the major peaks of the un-reacted  $\alpha\text{-Fe}_2\text{O}_3$  that disappear after sintering at  $500^\circ\text{C}$  (8 h).

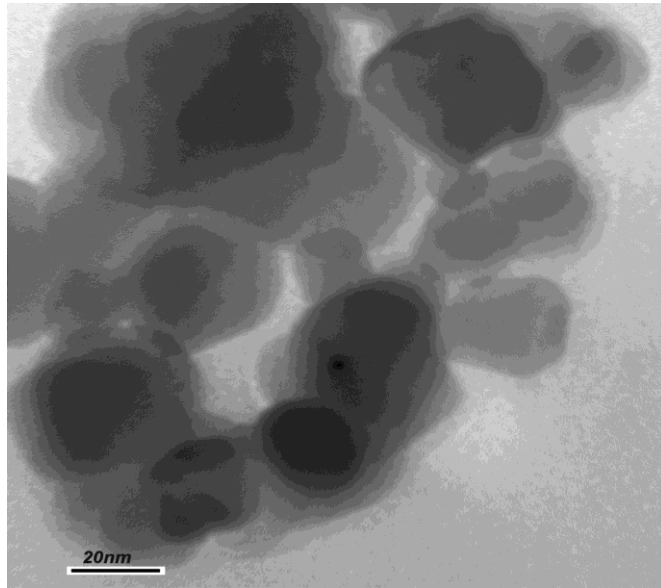


**Figure 5:** TEM image of the  $\text{EuCr}_{1-x}\text{Fe}_x\text{O}_3$  particles with  $x = 0.1$  showing typical particle size and morphology as those in the other nanoparticles.

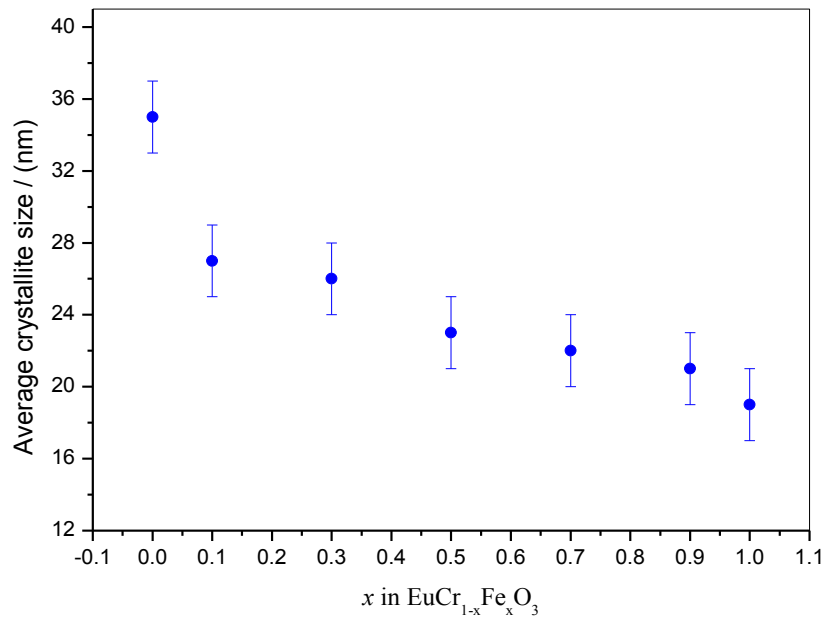


**Figure 6:** The variation of the average crystallite size of the  $\text{EuCr}_{1-x}\text{Fe}_x\text{O}_3$  nanoparticles with  $x$  (as estimated from the Scherrer equation).

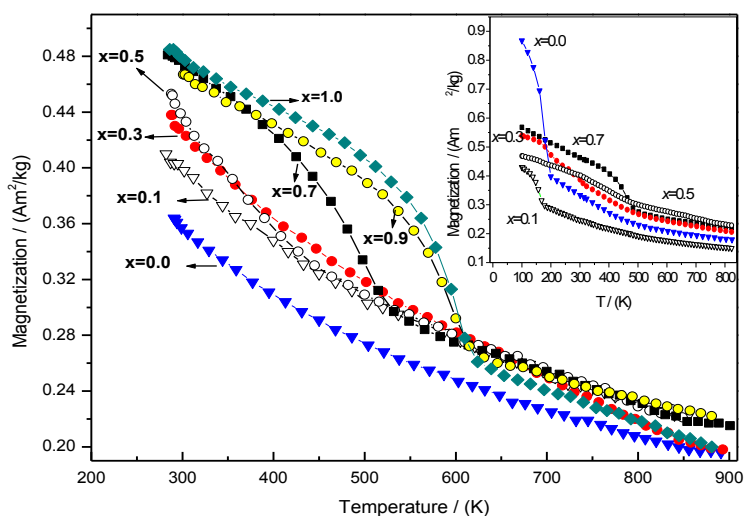


**Figure 7:** The magnetization ( $M$ ) vs. temperature for the  $\text{EuCr}_{1-x}\text{Fe}_x\text{O}_3$  nanoparticles recorded under an applied magnetic field of 1.5 T recorded using the Faraday balance. The inset shows the magnetization ( $M_s$ ) vs. temperature for the  $\text{EuCr}_{1-x}\text{Fe}_x\text{O}_3$  nanoparticles with  $x \leq 0.7$  recorded under an applied magnetic field of 1.35 T using the VSM.

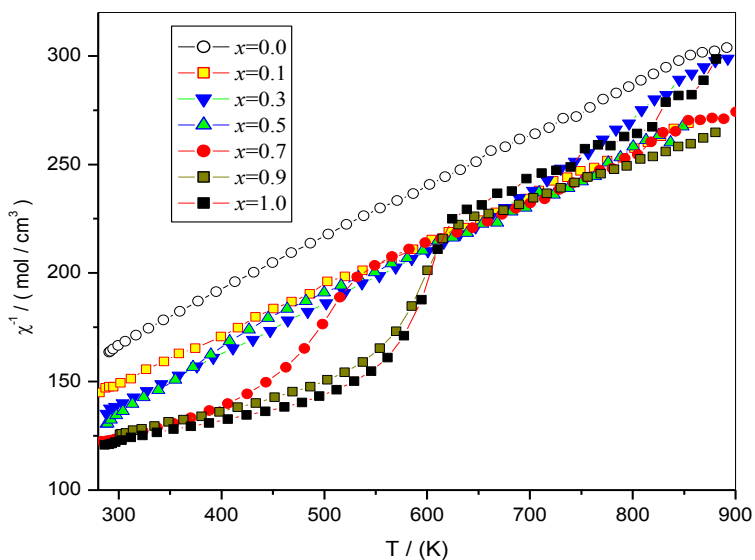


**Figure 8:** The temperature variation of the inverse (*total*) molar magnetic susceptibility ( $\chi^{-1}$ ) of the  $\text{EuCr}_{1-x}\text{Fe}_x\text{O}_3$  nanoparticles.

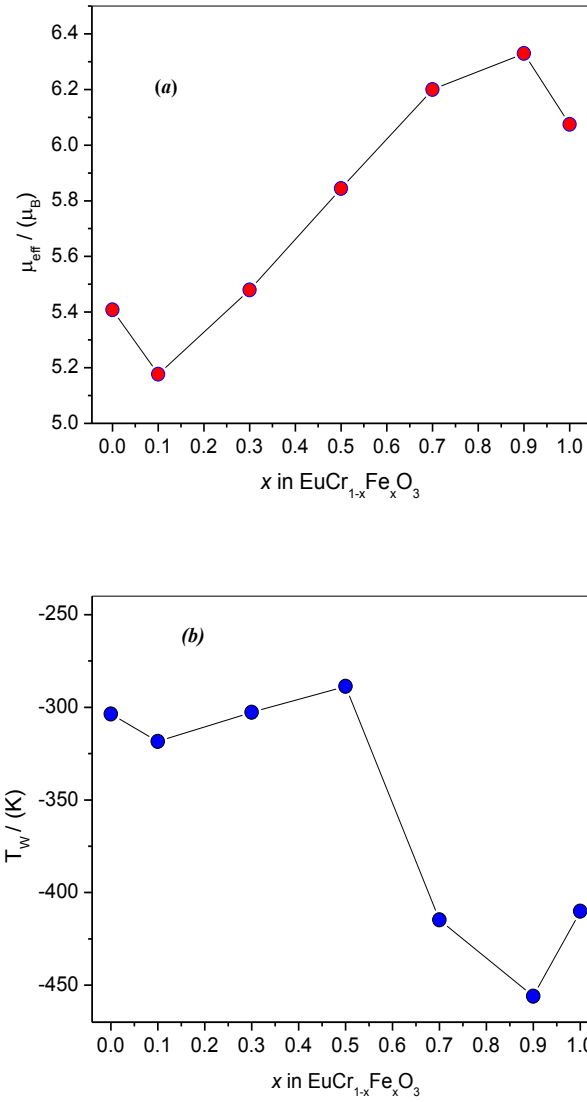


**Figure 9:** (a) The variation of the effective magnetic moment ( $\mu_{\text{eff}}$ ) per formula unit with  $x$ . (b) The variation of the Curie Weiss temperature  $T_W$  of the  $\text{EuCr}_{1-x}\text{Fe}_x\text{O}_3$  nanoparticles with  $x$ . These values are derived from the temperature variation of the inverse (*total*) paramagnetic susceptibility ( $\chi^{-1}$ ) assuming a pure Curie-Weiss behavior.

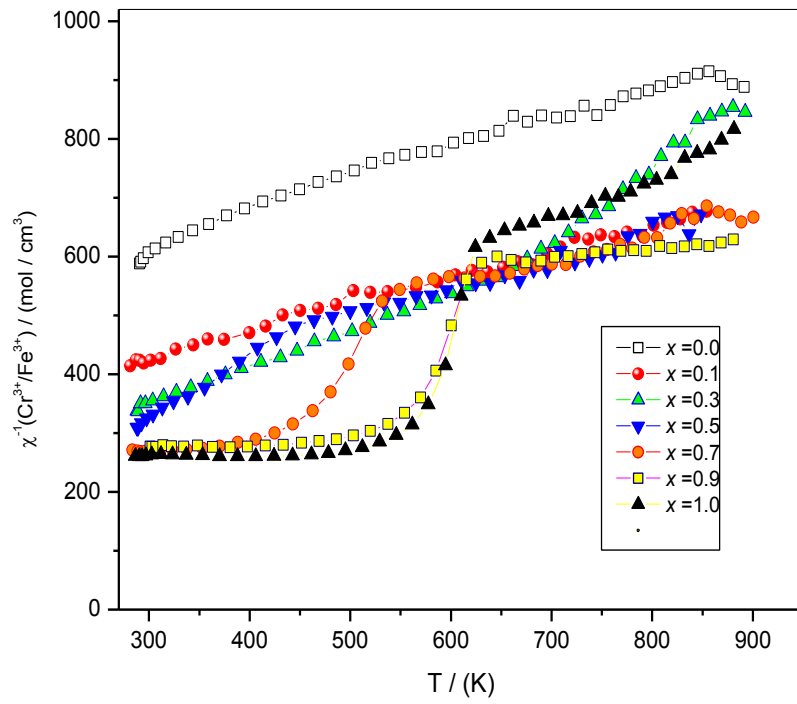


**Figure 10:** The temperature variation of the inverse magnetic susceptibility component  $\chi(\text{Cr}^{3+}/\text{Fe}^{3+})$  of the  $\text{EuCr}_{1-x}\text{Fe}_x\text{O}_3$  nanoparticles obtained using van Vleck formalism.

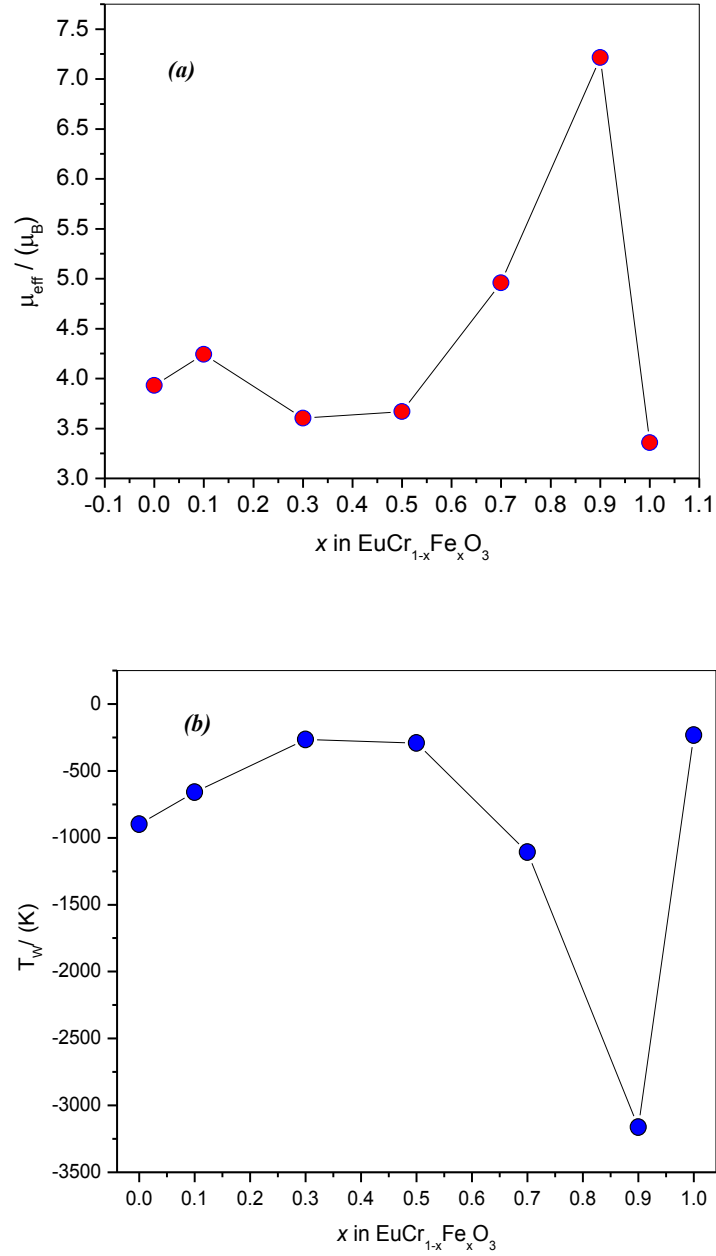


**Figure 11:** (a) The variation of the effective magnetic moment ( $\mu_{\text{eff}}$ ) per formula unit with  $x$ . (b) The variation of the Curie Weiss temperature  $T_W$  of the  $\text{EuCr}_{1-x}\text{Fe}_x\text{O}_3$  nanoparticles with  $x$ . These values are derived from the temperature variation of the inverse magnetic susceptibility component  $\chi(\text{Cr}^{3+}/\text{Fe}^{3+})$  of the  $\text{EuCr}_{1-x}\text{Fe}_x\text{O}_3$  nanoparticles obtained using the van Vleck formalism (see text).

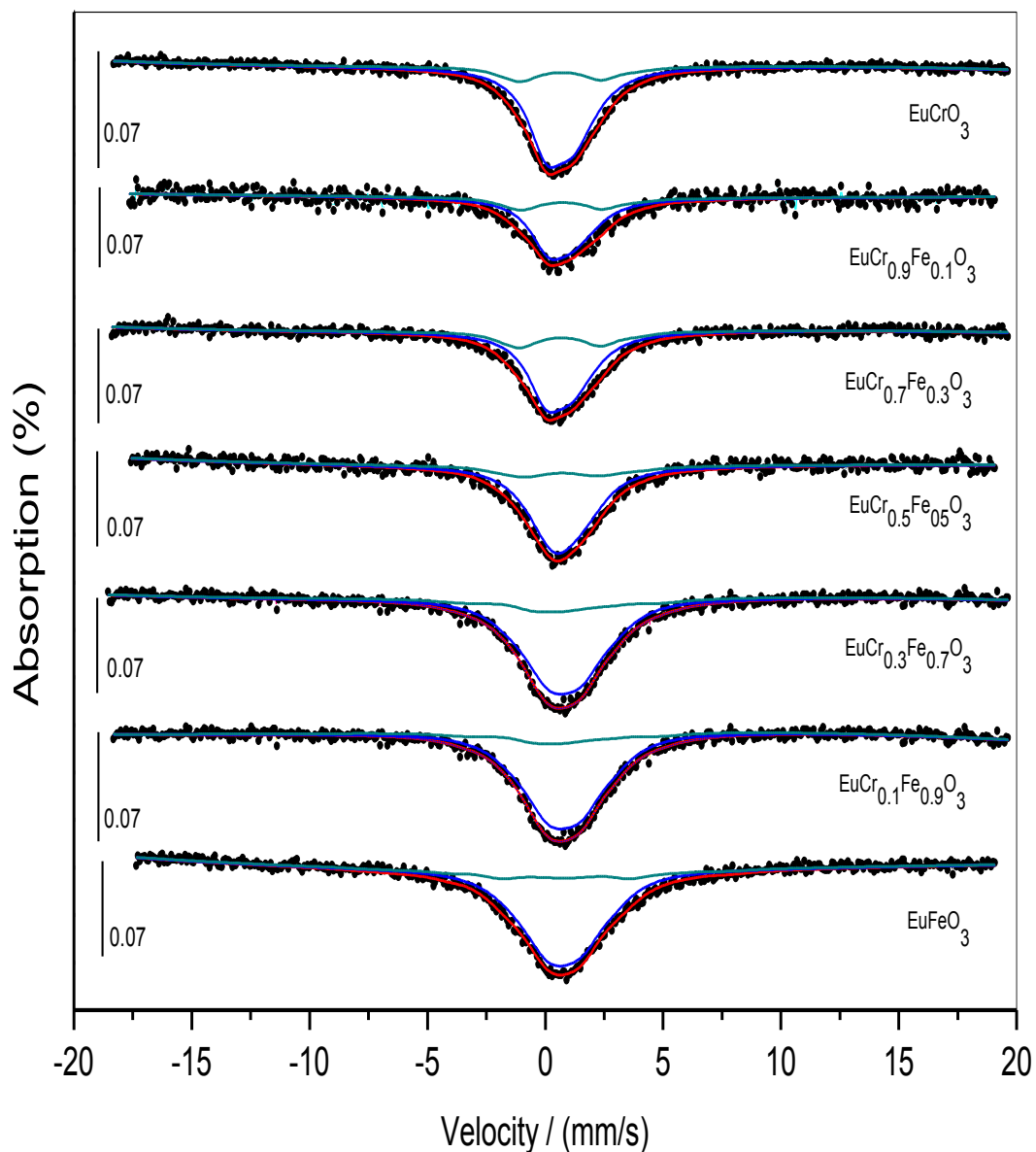


**Figure 12:** The  $^{151}\text{Eu}$  Mössbauer spectra recorded from the  $\text{EuCr}_{1-x}\text{Fe}_x\text{O}_3$  nanoparticles at 298K, fitted to two subcomponents according to the model explained in the text. The major and minor subcomponents are associated with  $\text{Eu}^{3+}$  ions at the A- and B-sites of the perovskite lattice, respectively.

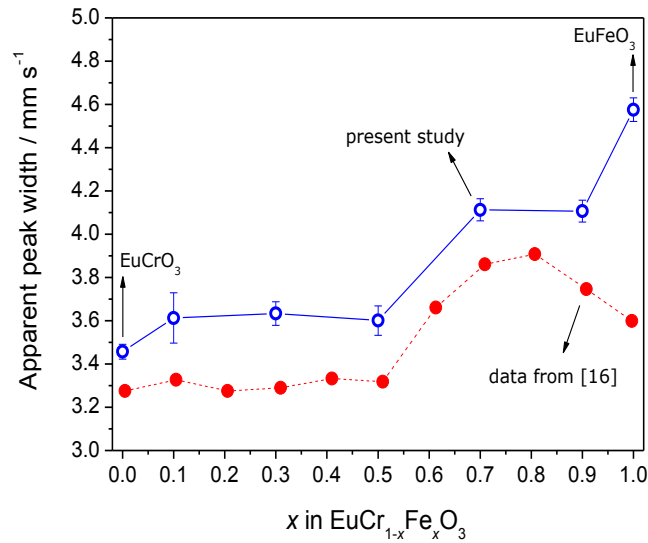


**Figure 13:** Apparent peak width observed by fitting the room temperature  $^{151}\text{Eu}$  Mössbauer spectra of the  $\text{EuCr}_{1-x}\text{Fe}_x\text{O}_3$  nanoparticles to a Lorentzian singlet (open circles) and corresponding data taken from [16] for the  $\text{EuCr}_{1-x}\text{Fe}_x\text{O}_3$  bulk counterparts (closed circles), as a function of  $x$ .

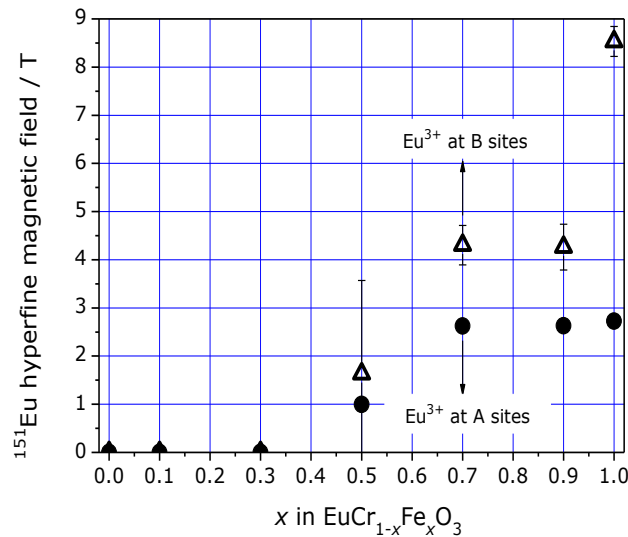


**Figure 14:** The hyperfine magnetic field detected at the  $^{151}\text{Eu}$  nuclei at A- (closed circles) and B-sites (open triangles) in  $\text{EuCr}_{1-x}\text{Fe}_x\text{O}_3$  as a function of  $x$ . The large error bar at  $x = 0.5$  belongs to the B-site hyperfine magnetic field data (open triangle), the standard deviation of the data characteristic to A-site europium ions being well represented by the size of the closed circles.

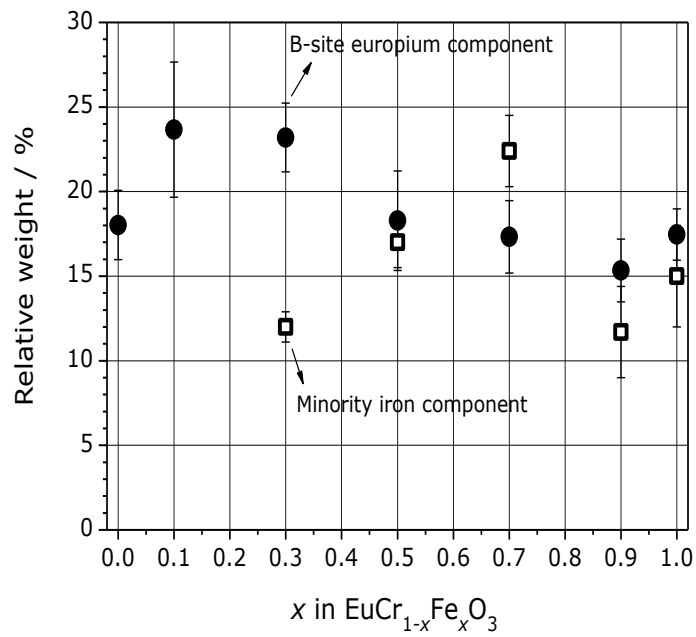


**Figure 15:** Relative area fraction of the  $^{151}\text{Eu}$  Mössbauer spectrum component attributed to B-site  $\text{Eu}^{3+}$  ions (closed circles), along with the estimated concentration of  $\text{Fe}^{3+}$  ions (open squares) associated with the minority component found in the corresponding  $^{57}\text{Fe}$  Mössbauer spectra recorded at 78 K [25] as a function of the  $x$  iron concentration.